The Antesonic Condition for the Explosion of Core-Collapse Supernovae I: Spherically Symmetric Polytropic Models: Stability & Wind Emergence

Matthias J. Raives,[1] Sean M. Couch[2,3,4,5],
Johnny P. Greco[6], Ondřej Pejcha[7], Todd A. Thompson[1,8],

[1]*Department of Astronomy, The Ohio State University, Columbus, OH 43210, USA*
[2]*Department of Physics and Astronomy, Michigan State University, East Lansing, Mi 48824, USA*
[3]*Department of Computational Mathematics, Science, and Engineering, Michigan State University, East Lansing, Mi 48824, USA*
[4]*National Superconducting Cyclotron Laboratory, Michigan State University, East Lansing, Mi 48824, USA*
[5]*Joint Institute for Nuclear Astrophysics, Michigan State University, East Lansing, Mi 48824, USA*
[6]*Department of Astrophysical Sciences, Princeton University, Princeton, NJ 08540, USA.*
[7]*Institute of Theoretical Physics,Faculty of Mathematics and Physics, Charles University, Prague, Czech Republic*
[8]*Center for Cosmology and Astroparticle Physics, The Ohio State University, Columbus, OH 43210, USA*

11 January 2018

ABSTRACT

Shock revival in core-collapse supernovae (CCSNe) may be due to the neutrino mechanism. While it is known that in a neutrino-powered CCSN, explosion begins when the neutrino luminosity of the proto-neutron star exceeds a critical value, the physics of this condition in time-dependent, multidimensional simulations are not fully understood. Pejcha & Thompson (2012) found that an 'antesonic condition' exists for time-steady spherically symmetric models, potentially giving a physical explanation for the critical curve observed in simulations. In this paper, we extend that analysis to more general time-dependent polytropic models. We verify the critical antesonic condition in our simulations, showing that models exceeding it drive transonic winds whereas models below it exhibit steady accretion. In addition, we find that (1) high spatial resolution is needed for accurate determination of the antesonic ratio and shock radius at the critical curve, and that low resolution simulations systematically underpredict these quantities, making explosion more difficult at lower resolution; (2) there is an important physical connection between the critical mass accretion rate at explosion and the mass loss rate of the post-explosion wind: the two are directly proportional at criticality, implying that, at criticality, the wind kinetic power is tied directly to the accretion power; (3) the value of the post-shock adiabatic index Γ has a large effect on the length and time scales of the post-bounce evolution of the explosion larger values of Γ result in a longer transition from the accretion to wind phases.

Key words: accretion, accretion disks – hydrodynamics – shock waves – supernovae: general

1 INTRODUCTION

When the iron core of a massive star collapses, the collapse is halted as the core exceeds nuclear densities, driving a shockwave into the infalling progenitor. This shockwave stalls, becoming a standing accretion shock at scales $r \sim 200\,\mathrm{km}$, and the progenitor continues to accrete onto the proto-neutron star (PNS) until the shock is revived by neutrino heating, leading to explosion, or until a black hole is formed (e.g., Bethe & Wilson 1985; Herant et al. 1994; Burrows et al. 1995; Janka & Müller 1995). Much of supernova theory is focused on understanding the revival of the stalled shock,

especially in 2D and 3D (Couch 2013; Dolence et al. 2015; O'Connor & Couch 2015). The idea of a critical neutrino luminosity for supernovae was first explored in Burrows & Goshy (1993) (hereafter, BG93). They showed that for a spherical, time-steady accretion flow with optically-thin neutrino heating and cooling, for a given accretion rate $\dot{M}_{\mathrm{acc}}$ there exists a critical core neutrino luminosity above which no steady-state accretion solution can be found. This work has since been extended to find 2-dimensional (2D) and 3-dimensional (3D), as well as time-dependent critical curves and critical surfaces (Murphy & Dolence 2017). Such stud-

ies have generally found that the 2D and 3D critical curves have a smaller normalization than the 1-dimensional (1D) curve; i.e., the critical luminosity for a given $\dot{M}_{\rm acc}$ is smaller in 2D and 3D than it is in 1D (but larger in 3D than in 2D) (Murphy & Burrows 2008; Couch 2013; Takiwaki et al. 2014). Furthermore, time-dependent studies have found radial (Fernández 2012; Gabay et al. 2015) and non-radial (Yamasaki & Yamada 2005; Yamasaki & Yamada 2007) instabilities such as the standing accretion shock instability (Blondin et al. 2003; Foglizzo et al. 2006; Murphy & Burrows 2008; Fernández & Thompson 2009; Fernández 2015) that may tend to lower the critical curve, potentially facilitating explosions.

In an effort to explain the existence of the critical neutrino luminosity of BG93, Pejcha & Thompson (2012) (hereafter, PT12) investigated the critical condition for explosion using a time-steady model, and with different levels of approximation for the post-shock microphysics and thermodynamics. For the simple toy model of pressureless free fall onto a standing shockwave and an isothermal post-shock medium, they found an analytic critical condition – the ratio of the isothermal sound speed to the escape velocity at the shock cannot exceed a critical threshold:

$$\xi_{\rm crit}^{\rm iso} \equiv \left.\frac{c_T^2}{v_{\rm esc}^2}\right|_{\rm shock} = \frac{3}{16}. \tag{1}$$

PT12 call this critical condition the 'antesonic condition,' because the condition is met at smaller radius than the sonic condition (in an isothermal wind, $c_T^2/v_{\rm esc}^2 = \frac{1}{4}$) is. We refer to the ratio of the sound speed squared to the escape velocity squared as the 'antesonic ratio,' which we denote as ξ.

PT12 extended their analysis to both time-steady polytropic models and models with a general equation of state and neutrino heating and cooling (i.e., the BG93 problem), numerically deriving antesonic conditions for each case. For polytropic models they numerically derive $\xi_{\rm crit}^{\rm poly} \simeq 0.19\Gamma$. In Appendix A, we provide an analytic derivation which shows that:

$$\xi_{\rm crit}^{\rm poly} \equiv \left.\frac{c_s^2}{v_{\rm esc}^2}\right|_{\rm max} = \frac{3}{16}\Gamma. \tag{2}$$

For the general case with neutrino heating and cooling, PT12 found that

$$\xi_{\rm crit}^{\nu} \equiv \left.\frac{c_s^2}{v_{\rm esc}^2}\right|_{\rm max} \simeq 0.19. \tag{3}$$

Here Γ is the adiabatic index, c_s is the adiabatic sound speed, and pressureless free-fall upstream of the shock is assumed. In these more general cases, the critical condition is on the maximum value of the antesonic ratio, which may or may not be at the shock radius. For models with neutrino heating and cooling, for example, the antesonic ratio reaches its maximum near the 'gain' radius (Pejcha & Thompson 2012), where neutrino heating balances cooling in the post-shock flow.

As shown by PT12, for the isothermal, polytropic, or general equation of state (EOS) with neutrino heating and cooling, or with any arbitrary changes to the heating and cooling physics, the physics of the antesonic condition is the same: above the critical antesonic ratio, it is impossible to simultaneously satisfy both the Rankine-Hugoniot shock-jump conditions and the spherically symmetric, time-steady Euler equations. PT12 associate the antesonic condition with a *dynamic* transition from steady spherical accretion to a transonic thermal wind, i.e., the supernova explosion.

Although PT12 provide an explanation for the critical curve, the applicability and utility of the critical condition has not been established in time-dependent or multidimensional simulations. However, the critical curve has been used to predict outcomes for large suites of massive star progenitors (Pejcha & Thompson 2015) in qualitative agreement with 1-dimensional time-dependent simulations tuned to produce explosions in 1987A-like progenitors (Ugliano et al. 2012; Ertl et al. 2016; Sukhbold et al. 2016). Even so, there is not yet a study that shows how the dynamical transition from accretion to explosion actually occurs in a time-dependent system, in the context of the antesonic condition.

In this paper, we take a step forward in understanding the nature of the critical curve in idealized, but time-dependent simulations, in order to better understand the nature of the transition from accretion to explosion that occurs when the antesonic ratio is exceeded – how this process behaves, how the structure of our model evolves – as a guide for full-physics simulations and as a test of our understanding of the physics in a simplified context. We adopt an approach similar to the model problems explored in PT12. In particular, we adopt a simplified, polytropic equation of state (EOS) in order to better understand the relevant physics in the accretion region, but we extend the results of PT12 to time-dependent simulations.

This paper is organized as follows. In section §2, we describe our computational methodology. In section §3, we present our results. In §3.1, we establish the applicability of the time-steady antesonic condition to our simulations – i.e., that models that exceed $\xi_{\rm crit}^{\rm poly}$ explode and that models that do not exceed $\xi_{\rm crit}^{\rm poly}$ do not. In §3.2, we show the resolution dependence of our simulations – specifically, we show that low resolution models underpredict $\xi_{\rm crit}^{\rm poly}$ and $R_{\rm sh}$ at the critical curve. In §3.3, we describe the properties of the transonic wind – in particular, how the wind mass loss rate is determined by the accretion rate at explosion – which establishes an explicit connection between the accretion power at the shock and the energy of the explosion. In §3.4, we describe the emergence of a wind-driven shell as the wind sweeps up the accreting matter. In §3.5, we explore the effects of time-dependent perturbations to the simulations, i.e., whether a model can explode when it only temporarily exceeds the critical curve. In §4, we provide a brief conclusion.

2   METHODOLOGY

Our study consists of a set of 1D, spherically symmetric hydrodynamics simulations. The time evolution of the system is governed by the hydrodynamic equations:

$$\frac{\partial \rho}{\partial t} + \frac{1}{r^2}\frac{\partial(r^2 \rho v_r)}{\partial r} = 0, \tag{4}$$

$$\frac{\partial(\rho v_r)}{\partial t} + \frac{\partial(\rho v_r^2)}{\partial r} + \frac{1}{\rho}\frac{\partial P}{\partial r} + \frac{GM}{r^2} = 0, \tag{5}$$

where ρ is the gas density, v_r is the radial velocity, P is the gas pressure, G is the gravitational constant, and $M =$
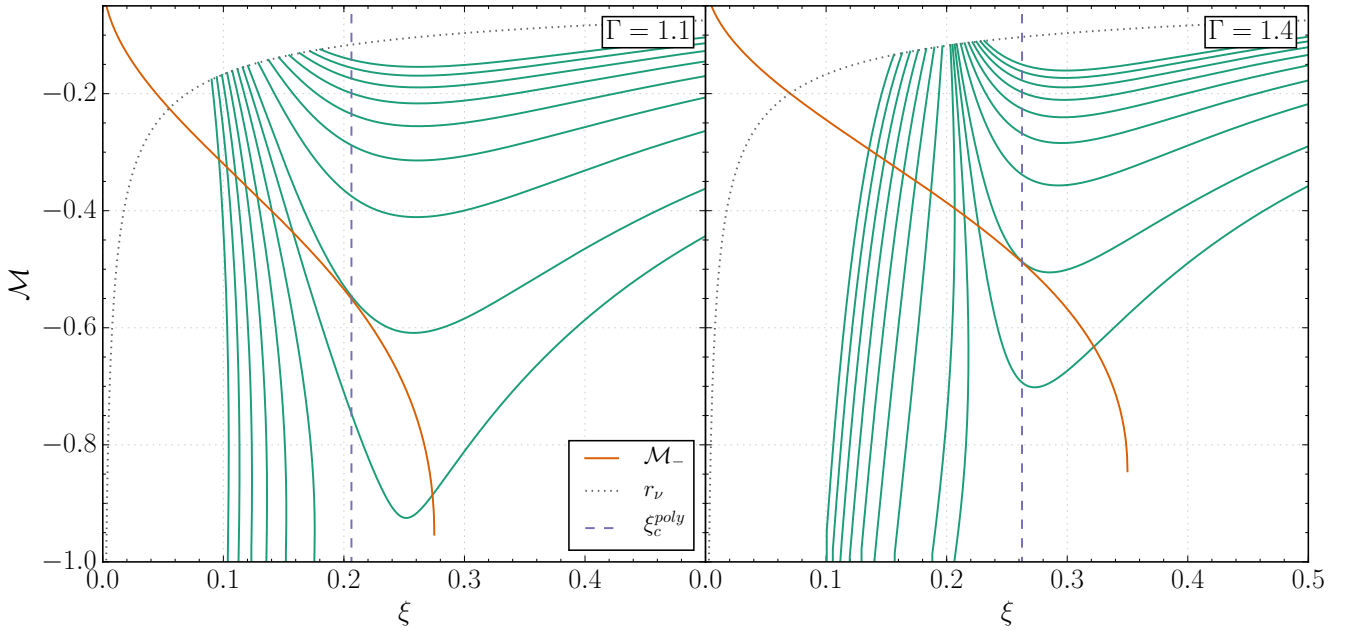
Figure 1. Solutions to the time-steady Euler equations, plotted as the Mach number $\mathcal{M}$ versus the antesonic ratio ξ, for $\Gamma = 1.1$ (left) and $\Gamma = 1.4$ (right). The dashed gray curve shows the neutrinosphere radius r_ν. The green curves correspond to configurations with different choices of K at fixed $\dot{M}_{\rm acc}$. The orange curve shows the Mach number $\mathcal{M}_-$ immediately downstream of the shock (Equation 11); the shock is located where the green and orange curves intersect. The critical K for a given $\dot{M}_{\rm acc}$ is the K such that the resultant velocity profile is tangent to the post-shock Mach number curve at the point of intersection. Velocity profiles that do no intersect the $\mathcal{M}_-$ curve do not have an accretion shock, and thus are not considered here. Some profiles have two points of intersection with the $\mathcal{M}_-$ curve; in these cases, the shock is located at the first intersection (i.e., the intersection at smaller ξ, and therefore r).

$1.4 \rm M_\odot$ is the mass of the central PNS; we do not consider the self-gravity of the gas in our simulations. We use a simple, polytropic EOS for the flow downstream of the shock:

$$P = K\rho^\Gamma \qquad (6)$$

where $\Gamma = 1.1, 1.4$ is the adiabatic index and K is a normalization factor. We solve the hydrodynamics equations with the FLASH[1] code (Fryxell et al. 2000). Our fiducial simulations use the directionally unsplit hydrodynamics solver, third-order piecewise parabolic spatial reconstruction, the 'hybrid' slope limiter, and the LLF Riemann solver (we discuss alternate hydro solvers in §3.2). The fiducial simulations were run on a grid with inner radius $x_{\rm min} = r_\nu = 30\,\rm km$ and outer radius $x_{\rm max} = 5000\,\rm km$, with a minimum grid spacing $\delta x \approx 0.607\,\rm km$, obtained using a maximum of 8 AMR refinement levels. The effects of numerical resolution on our results are explored in more detail in §3.2.

Inside the shock radius, the gas is initialized to the steady-state velocity and density profiles determined in PT12. These profiles are defined by K, Γ and the mass accretion rate $\dot{M}_{\rm acc}$. The conditions at the shock are described by the Rankine-Hugoniot shock-jump conditions:

$$\rho_- v_- = \rho_+ v_+ \qquad (7)$$

$$\rho_- v_-^2 + P_- = \rho_+ v_+^2 + P_+, \qquad (8)$$

where $+$ and $-$ denote quantities just upstream and just

downstream of the shock, respectively. We use just these two conditions, neglecting the enthalpy condition, because our choice of K both upstream and downstream of the shock (see below) fixes the compressibility and entropy of the post-shock medium, rendering the enthalpy condition moot. In a self-consistent calculation with neutrino heating and cooling, the enthalpy of the immediate post-shock medium would be determined by the full set of shock-jump conditions. Our use of a polytropic EOS with prescribed post-shock K obviates the need for the third shock-jump condition and allows us to control the thermal properties of the accreting material by hand.

Outside the shock radius, the density and velocity of the gas are set by the equations of pressureless free-fall:

$$v_+(r) = \sqrt{\frac{2GM}{r}}, \qquad (9)$$

$$\rho_+(r) = \frac{\dot{M}_{\rm acc}}{4\pi r^2 v(r)} = \frac{\dot{M}_{\rm acc}}{4\pi r^{3/2}} \frac{1}{\sqrt{2GM}}. \qquad (10)$$

For numerical reasons, instead of using $P_+ = 0$, we switch from a small but finite K upstream of the shock to a large, specified, K downstream of the shock. The relevant solution to the shock-jump conditions (assuming $P_+ = 0$) is then:

$$\mathcal{M}_- \equiv \frac{v_-}{c_s} = \frac{1}{2}\left(\sqrt{\frac{1}{\xi} - \frac{4}{\Gamma}} - \sqrt{\frac{1}{\xi}}\right), \qquad (11)$$

where all quantities are evaluated just downstream of the

---

[1] Available for download at www.flash.uchicago.edu.

shock. Here, ξ is the local antesonic ratio,

$$\xi = \frac{c_s^2}{v_{\rm esc}^2} = \frac{K\Gamma\rho^{\Gamma-1}r}{2GM}, \qquad (12)$$

as opposed to the critical antesonic ratio $\xi_{\rm crit}$, which is the *maximum* value of the antesonic ratio (see Equation 2).

We show the time-steady solutions to this problem (Equation 4 and Equation 5 with $\Gamma = 1.1, 1.4$) in Figure 1. The solid green lines correspond to different values of K in the post-shock medium, and the solid orange line is the Mach number just downstream of the shock, given in Equation 11. For a given profile, the shock exists at the intersection between the green an orange curves. For cases where two points of intersection exist, the shock is located at the interior one, i.e., at smaller ξ, and thus smaller r at fixed K (Pejcha & Thompson 2012).

In all of our simulations, we begin by specifying $K, \dot{M}_{\rm acc}$ from a grid of values spaced linearly in K and logarithmically in $\dot{M}_{\rm acc}$, in the interval $0.1\ {\rm M}_\odot\ {\rm s}^{-1} \leqslant \dot{M}_{\rm acc} \leqslant 1.06$ ${\rm M}_\odot\ {\rm s}^{-1}$. This choice defines the initial, time-steady, density and velocity profiles. We allow the system to equilibrate for $0.1\,{\rm s}$, then decrease the mass accretion rate by a factor $f_{\dot{M}}$ (which may be equal to 1) for a time $\Delta t_{\dot{M}}$ (which may be equal to the total simulation length). The full simulation length is $2.0\,{\rm s}$.

3 RESULTS

3.1 The Antesonic Condition

We first reproduce an approximation of the PT12 critical curve, as shown in Figure 2. We start the simulations at some stable accretion rate $\dot{M}_{\rm acc,0}$, which we then decrease by constant factors $f_{\dot{M}}$ at the outer boundary. For $(\dot{M}, K)$ configurations that lie below the critical curve, the simulations maintain the initial conditions, displaying time-steady accretion solutions. As we move the simulations to configurations that lie above the critical curve by decreasing $\dot{M}_{\rm acc}$, they undergo dynamical transformations to time-steady wind solutions. We identify the wind solutions with successful supernova explosions.

For the unstable configurations, we investigate the time required for explosion. As there is no unique, well-defined way to identify the time for the onset of explosion, we consider three such definitions. $t_{\rm ante}$ is defined to be the first time for which $\xi > \xi_{\rm crit}^{\rm poly}$ (see Equation 2); we use this timescale as a physically motivated definition of $t = 0$. $t_{\rm wind}$ is defined as the first time for which the fluid velocity immediately downstream of the shock is positive. t_{400} is defined to be the time at which the shock reaches a fixed radius $r = 400$ km. Though this definition is more arbitrary than the other two, it mirrors definitions used in the literature, e.g., Couch (2013). For comparison, we also consider $t_{\rm sonic}$, the time at which the wind first achieves $\mathcal{M} = 1$.

We plot the velocity profiles of the simulation at these times in Figure 3. Though the $\Gamma = 1.4$ case is larger in physical extent than the $\Gamma = 1.1$ case, the velocity profiles are otherwise similar. The t_{400} profile is not shown for the $\Gamma = 1.4$ case, as it coincidentally overlaps with the $t_{\rm ante}$ profile.

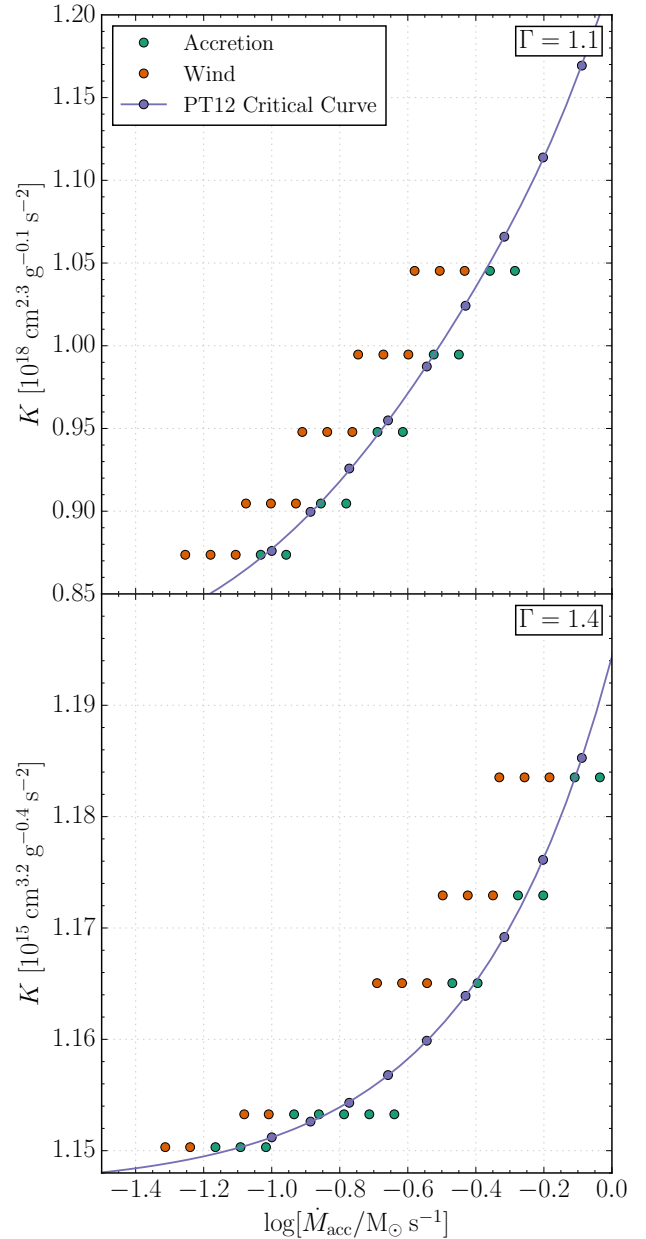Finally, we also plot the (maximum) value of the an-

Figure 2. The critical curve for our parametrized supernova model, for $\Gamma = 1.1$ (left) and $\Gamma = 1.4$ (right). For a given accretion rate $\dot{M}_{\rm acc}$, values of K above a certain critical value result in a wind solution we identify with a supernova. In our simulations, we hold K fixed and reduce $\dot{M}_{\rm acc}$ to achieve the same result. We note that, for $\Gamma = 1.4$, some configurations that lie above the critical curve do not explode; we attribute this to the resolution dependence of the critical curve (see §3.2 for more details).

tesonic ratio as a function of time in Figure 4.[2] We include

---

[2] The slight decrease in $\max(\xi)$ at $t \sim -0.03$ is due to the shock colliding with the trailing end of the $f_{\dot{M}}$ perturbation, which spreads out over many radial zones, and is steeper than the leading end. The sharp change in $\dot{M}$ manifests as a sharp change in ρ, which is visible in ξ as $\xi \propto \rho^{\Gamma-1}$.
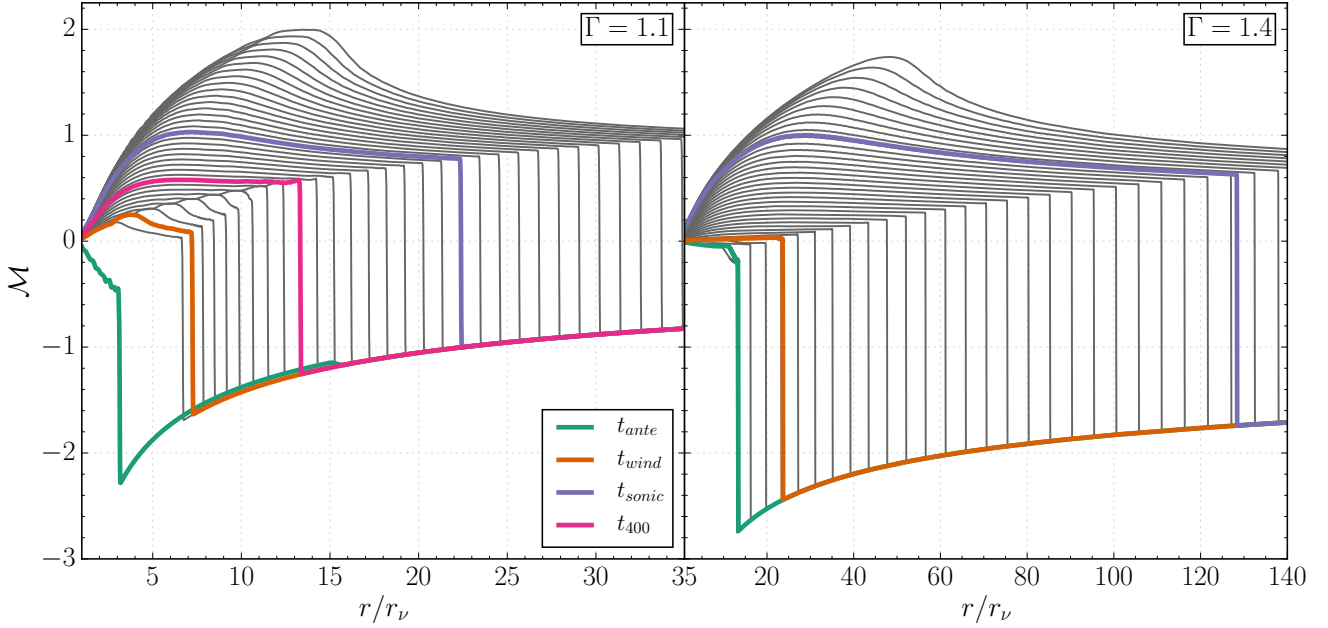
Figure 3. Velocity profiles for $\dot{M}_{\mathrm{acc},0} = 1.06\,\mathrm{M}_\odot\,\mathrm{s}^{-1}$, with $\Gamma = 1.1$ (left) and $\Gamma = 1.4$ (right) cases, with the profiles corresponding to t_{wind}, t_{ante}, and t_{400} highlighted. Output profiles are separated in time by 1 ms in the $\Gamma = 1.1$ case, and 20 ms in the $\Gamma = 1.4$ case. The profile at $t = t_{400}$ is not shown for $\Gamma = 1.4$, as the initial shock radius is near 400 km. For $\Gamma = 1.1$, see Figure 10 and §3.3, §3.4 for further evolution of the wind.

markers at the three time-scales (t_{400}, t_{wind}, and t_{sonic}) identified above. Not only does the explosion evolve much more slowly for $\Gamma = 1.4$ than $\Gamma = 1.1$, it does not reach as large of an antesonic ratio as the $\Gamma = 1.1$ explosion does.

3.2 Resolution Dependence

Here we investigate the effect of increasing resolution on our ability to resolve the shock radius, the antesonic ratio, and the critical curve. We measure the resolution of the study with the *minimum* grid spacing, δx, which can be decreased by either changing the linear or adaptive refinement:

$$\delta x = \frac{x_{\max} - x_{\min}}{b \times n \times 2^{\ell-1}} = \frac{621.25\ \mathrm{km}}{n \times 2^\ell}, \tag{13}$$

where n is the level of linear refinement, $b = 16$ is the block size, and ℓ is the maximum number of AMR refinement levels.

In Figure 5, we show the effect of increasing resolution (decreasing δx) on the fidelity of our simulations, as measured by the accuracy of the shock radius R_{sh} and the critical antesonic ratio relative to the value found by PT12. We also show how this effect changes at various distances from the critical curve, defined as:

$$\delta K \equiv \left| \frac{K}{K_{\mathrm{crit}}} - 1 \right| \tag{14}$$

where K_{crit} is the critical value of K for the specified $\dot{M}_{\mathrm{acc}}$.

We find that under-resolved simulations systematically underpredict R_{sh} and ξ_{sh} and overestimate the critical curve, compared to the semi-analytic PT12 result. Within the context of our simulations, this means that less well-resolved

calculations will be more stable (less susceptible to explosion) than more highly resolved simulations. Furthermore, simulations near the critical curve require higher resolution in order to calculate the shock radius to a given accuracy. That is to say, at fixed physical resolution, configurations closer to the critical curve are less well resolved than configurations further away from the critical curve.

For example, a simulation on the critical curve ($\delta K \simeq 0$) with resolution $\delta x = 0.607$ km measures the antesonic ratio to about 15 per cent accuracy and the shock radius to about 20 per cent accuracy for $\Gamma = 1.1$. For $\Gamma = 1.4$, $\delta x = 0.607$ km yields an accuracy of about 45 per cent in R_{sh} and 15 per cent in ξ_{sh}). Whereas, a simulation of the same resolution but displaced from the critical curve by $\delta K = 7.7 \times 10^{-2}$ measures the antesonic ration to about 5 per cent accuracy and the shock radius to better than 1 per cent accuracy.

In Figure 6, we show the effect of resolution of the critical curve itself (compare to the top panel of Figure 2). We see that, at low resolution, configurations can be above the PT12 critical curve but still yield accretion solutions, whereas at high resolution, these configurations yield wind solutions as expected. This potentially explains why we see accretion solutions above the critical curve in Figure 2 (for $\Gamma = 1.4$.

We perform a more limited version (specifically, $\Gamma = 1.1$ only, and with fewer choices of δx) of this analysis for the HLL and HLLC hydro solvers, to ensure that our choice of solver does not unduly affect our results. We find that these solvers yield statistically equivalent values of $R_{\mathrm{sh}}/R_{\mathrm{sh},0}$ and $\xi_{\mathrm{sh}}/\xi_{\mathrm{sh},0}$ at $\delta x \lesssim 1.2$ km. At $\delta x \gtrsim 1.2$ km, the LLF solver yields higher accuracy in $R_{\mathrm{sh}}/R_{\mathrm{sh},0}$ and $\xi_{\mathrm{sh}}/\xi_{\mathrm{sh},0}$ by factors of approximately 1.5 and 2, respectively. The critical curves
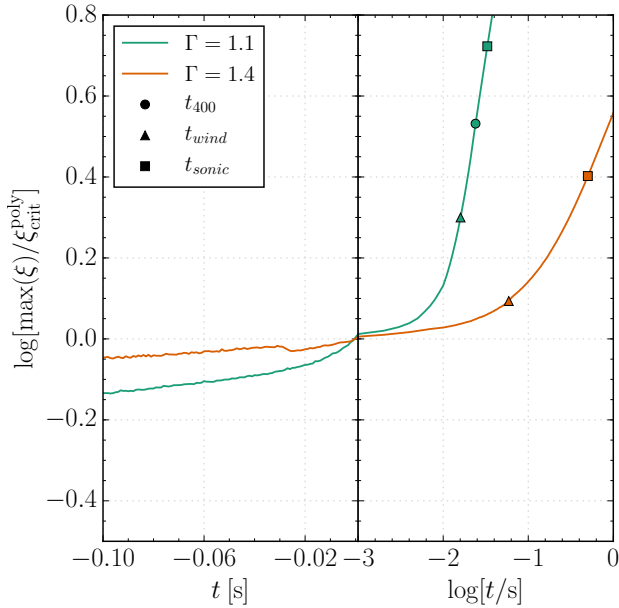
Figure 4. The maximum antesonic ratio vs. time for a configuration with $\dot{M}_{\rm acc,0} = 1.06\,{\rm M}_\odot\,{\rm s}^{-1}$, for both $\Gamma = 1.1$ and $\Gamma = 1.4$. For comparison, the time-scales t_{400}, $t_{\rm wind}$, and $t_{\rm sonic}$ are also shown for each configuration. The time-scale is normalized such that $t_{\rm ante} = 0$; the left panel shows $t < 0$ on a linear scale, while the right panel shows $t > 0$ on a log scale. The growth of the antesonic ratio starts out slow in both cases, but quickly increases. The $\Gamma = 1.1$ simulation shows both a faster increase in $\xi/\xi_{\rm crit}$ and a larger maximum $\xi/\xi_{\rm crit}$.

produced with these solvers (i.e., in figures analogous to Figure 6) are identical at (a given δx) under all three solvers.

For context, we compare these results to the resolutions used in recent 3D simulations. (Takiwaki et al. 2012) uses logarithmically spaced zones, with a fractional resolution of $\frac{\delta x}{x} \simeq 0.02$ (this corresponds to a linear resolution $\delta x = 2$ km at a radius of 100 km). Lentz et al. (2015) and Fernández (2015) use smaller fractional resolutions, $\frac{\delta x}{x} \simeq 0.014$ and $\frac{\delta x}{x} \simeq 0.0045$ respectively (corresponding to linear resolutions 1.4 km and 0.45 km, respectively, at a radius of 100 km). Couch & Ott (2013) use a maximum resolution of 0.49 km, and Radice et al. (2016) perform a resolution study for resolutions up to 0.191 km (though they do not run a full simulation at this resolution due to the high computational cost). While not an exhaustive list of the past decade of supernova simulations, these selected studies indicate that 3D supernova simulations are typically not run at resolutions fine enough for convergence of $R_{\rm sh}$ or $\max(\xi_{\rm crit}^{\rm poly})$ to 10 per-cent near the critical curve.

3.3 The Transonic Wind

Once the accretion flow exceeds the antesonic limit, it begins a time-dependent transition to a transonic wind, shown by the profiles in between the green and blue curves in Figure 3. In Figure 7, we plot the wind mass loss rate $\dot{M}_{\rm wind}$ against the initial accretion rate of the profile $\dot{M}_{\rm acc,0}$. We find that for configurations corresponding to initial conditions on the

critical curve, $\dot{M}_{\rm wind}$ and $\dot{M}_{\rm acc,0}$ are tightly correlated – their ratio is very nearly constant. Furthermore, simulations with the same initial accretion rate $\dot{M}_{\rm acc,0}$, but different decreases in $\dot{M}_{\rm acc}$, specified by $f_{\dot{M}}$, yield winds with the same $\dot{M}_{\rm wind}$.

This point is most clear when we look at initial conditions that lie significantly below the critical curve (i.e., configurations with the same $\dot{M}_{\rm acc,0}$, but a smaller K). These configurations are displaced from the $\dot{M}_{\rm wind}$ – $\dot{M}_{\rm acc,0}$ correlation of the higher K configurations in the sense that they have significantly smaller wind mass loss rates than the higher K configurations. However, when we investigate how the wind mass loss rate depends on K, we find that both the high K and low K configurations lie along the same relation. That is to say, the properties of the wind are determined by the thermal properties of the model (i.e., the EOS parameters K and Γ) rather than the accretion rate as specified by $\dot{M}_{\rm acc}$.

Naively, one might not expect such a tight correspondence between $\dot{M}_{\rm wind}$ and $\dot{M}_{\rm acc,0}$. The tight correlation between $\dot{M}_{\rm wind}$ and K, on the other hand, is to be expected for a thermally driven wind with a polytropic EOS. To see this, note that the steady-state wind mass loss rate can be written as

$$\dot{M}_{\rm wind} = 4\pi R_{\rm sonic}^2 c_s \rho(R_{\rm sonic}) = {\rm constant}, \qquad (15)$$

where

$$R_{\rm sonic} = \frac{GM}{2c_s^2} \qquad (16)$$

is the radius of the sonic point. Using this relation, and the equation of state, we can write:

$$\dot{M}_{\rm wind} = \frac{\pi G^2 M^2}{(K\Gamma)^{1/(\Gamma-1)}} c_s^{(4-3\Gamma)/(\Gamma-1)} \qquad (17)$$

Similarly, we can write the mass accretion rate (which is constant everywhere) as

$$\dot{M}_{\rm acc} = 4\pi R_{\rm sh}^2 v(R_{\rm sh})\rho(R_{\rm sh}), \qquad (18)$$

where we can use the critical condition to write the shock radius $R_{\rm sh}$ as

$$R_{\rm sh} = \frac{3GM\Gamma}{8c_s^2}. \qquad (19)$$

We can also use Equation 11 to write the velocity at the shock as

$$v(R_{\rm sh}) = \mathcal{M}_- c_s = \frac{1}{\sqrt{3\Gamma}} c_s, \qquad (20)$$

and thus write:

$$\dot{M}_{\rm acc} = -\frac{3\sqrt{3}\pi}{16} \frac{G^2 M^2 \Gamma^{3/2}}{(K\Gamma)^{1/(\Gamma-1)}} c_s^{(4-3\Gamma)/(\Gamma-1)}. \qquad (21)$$

Thus the ratio of the mass loss rate to the mass accretion rate is:

$$\left|\frac{\dot{M}_{\rm wind}}{\dot{M}_{\rm acc}}\right| = \frac{16}{3\sqrt{3}} \frac{1}{\Gamma^{3/2}} \left(\frac{c_s(R_{\rm sonic})}{c_s(R_{\rm sh})}\right)^{(4-3\Gamma)/(\Gamma-1)} \qquad (22)$$

For $\Gamma = 1.1$, this is approximately:

$$\left|\frac{\dot{M}_{\rm wind}}{\dot{M}_{\rm acc}}\right| \simeq 2.7 \left(\frac{c_s(R_{\rm sonic})}{c_s(R_{\rm sh})}\right)^7 = 2.7 \left(\frac{\rho(R_{\rm sonic})}{\rho(R_{\rm sh})}\right)^{0.35} \qquad (23)$$
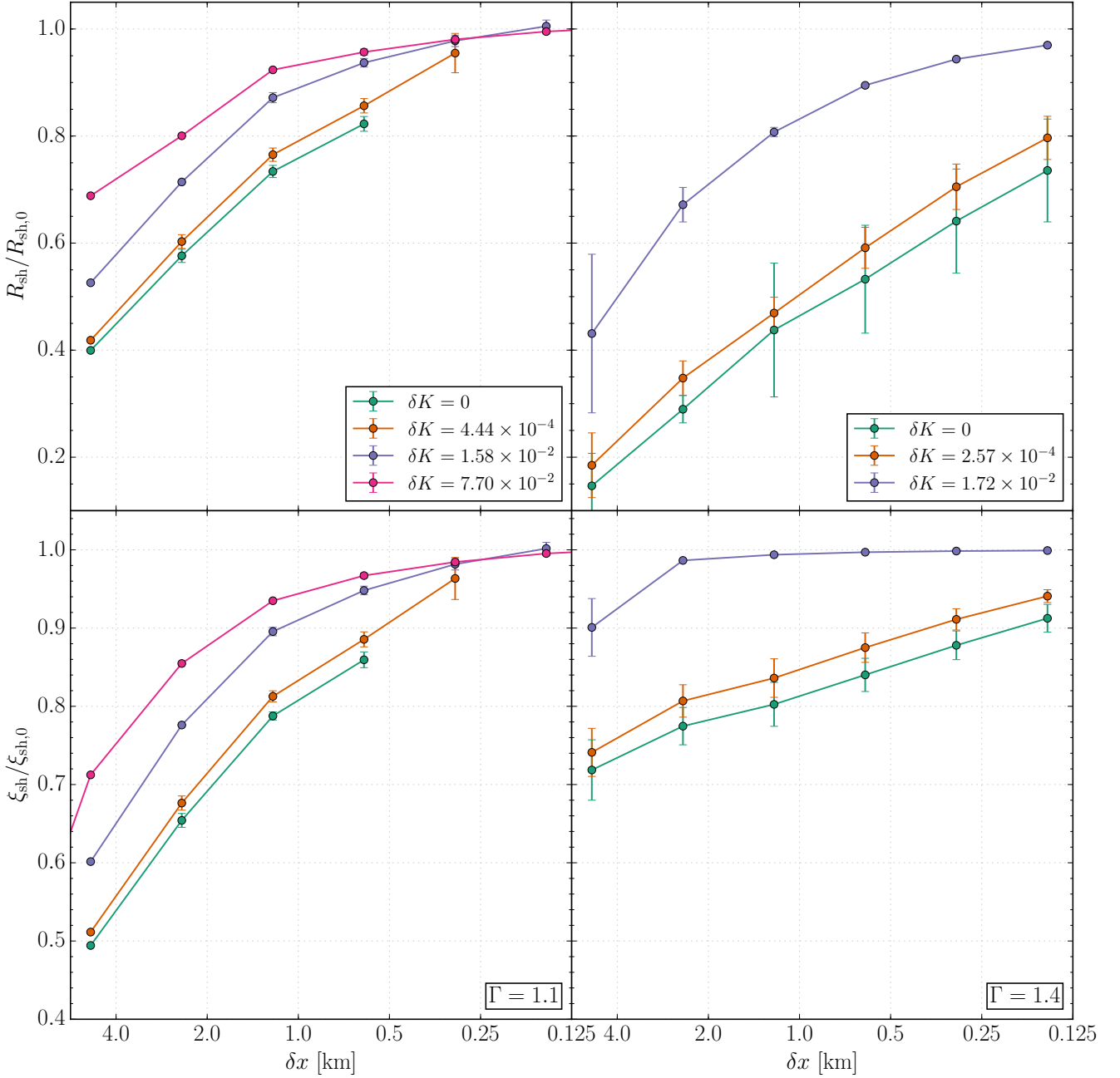
Figure 5. Shock radius (top) and antesonic ratio at the shock (bottom), relative to the PT12 value, for simulations at various distances from the critical curve, for $\Gamma = 1.1$ (left) and $\Gamma = 1.4$ (right), and with fixed $\dot{M} = 0.37\,\mathrm{M}_\odot$. We see that simulations close to the critical curve require higher resolution to converge to the same accuracy compared to those further away. Furthermore, $\Gamma = 1.4$ simulations require higher resolution to achieve a similar accuracy in R_{sh} to $\Gamma = 1.1$ simulations.

and for $\Gamma = 1.4$:

$$\left|\frac{\dot{M}_{\mathrm{wind}}}{\dot{M}_{\mathrm{acc}}}\right| \simeq 1.9 \left(\frac{c_s(R_{\mathrm{sonic}})}{c_s(R_{\mathrm{sh}})}\right)^{-1/2} = 1.9 \left(\frac{\rho(R_{\mathrm{sonic}})}{\rho(R_{\mathrm{sh}})}\right)^{-0.1} \tag{24}$$

While the antesonic condition occurs before the sonic point in the flow, the conditions are relatively similar (Equation 16 can be written as $\xi = \frac{1}{4}$, in comparison to $\xi = \frac{3\Gamma}{16} \sim 0.2$ at the shock). Thus we should expect the sound speed at the

shock to be very similar to that at the sonic point. Alternatively, we could consider the small exponent on the density in the alternate form of this relation – even for an order of magnitude difference in density, the ratio of $\dot{M}_{\mathrm{wind}}$ to $\dot{M}_{\mathrm{acc}}$ is still of order unity.

The implication of the result that $\dot{M}_{\mathrm{wind}} \sim \dot{M}_{\mathrm{acc}}$ is that, when the antesonic condition is met, the kinetic power of the resulting wind $\dot{E}_{\mathrm{wind}} = \frac{1}{2}\dot{M}_{\mathrm{wind}}v^2(R_{\mathrm{sonic}})$ is proportional to the accretion luminosity at the shock $\dot{E}_{\mathrm{acc}} = \frac{1}{2}\dot{M}_{\mathrm{acc}}v^2(R_{\mathrm{sh}})$
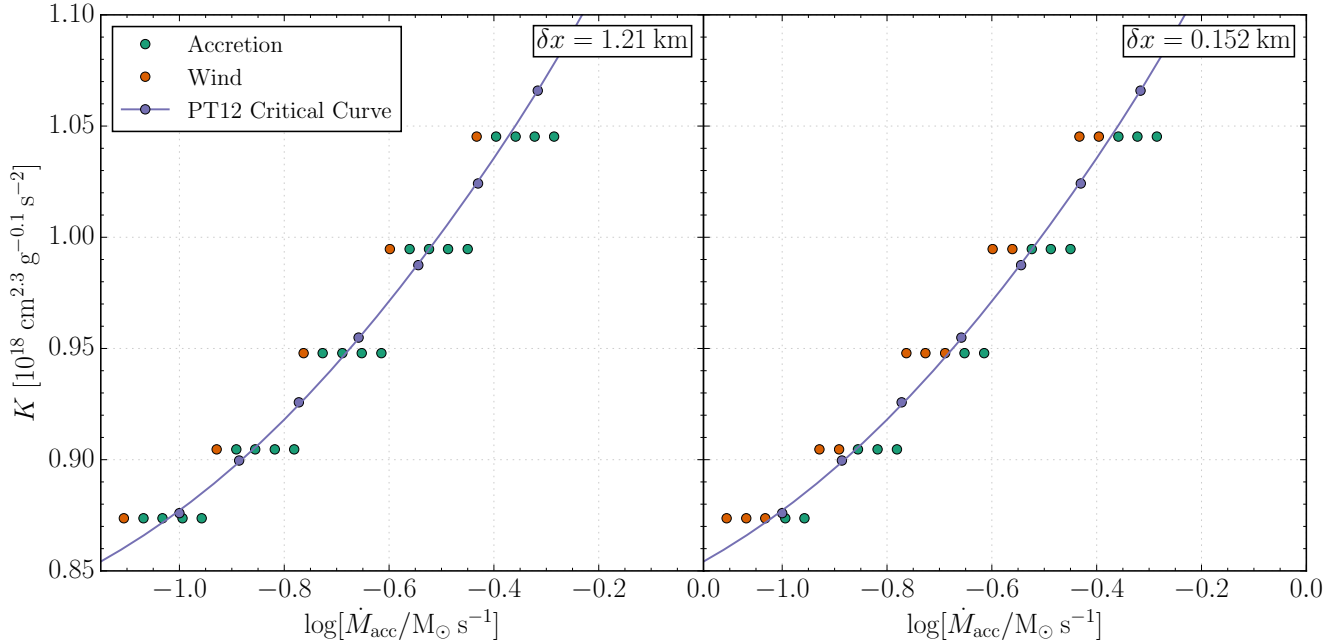
Figure 6. The critical curve at 2 different resolutions, for $\Gamma = 1.1$. We see that underresolved simulations have a critical curve that has a larger normalization than the PT12 result; as resolution increases the critical curve normalization approaches the PT12 value.

moments before explosion. In actuality, this sets the initial conditions for subsequent time evolution of the wind, which decreases in power as the PNS core cools, but such cooling is not considered in this paper. This approximate equivalence between $\dot{E}_{acc}$ and $\dot{E}_{wind}$ is demonstrated in Figure 8. We stress that the simulations that explode with the highest $\dot{M}_{acc}$ are also those with the highest $\dot{E}_{wind}$. This implies that, for fixed progenitor properties, explosions with the largest accretion rates will have the highest energy explosions, and thus have larger nickel yields. Because $\dot{M}_{acc}$ is a monotonically decreasing function of time for a real massive star progenitor, and because the neutron star mass grows monotonically throughout the quasi-static accretion phase, this implies that – all else equal – explosions at higher $\dot{M}_{acc}$ produce neutron star remnants of smaller mass, as found in Pejcha & Thompson (2015) in their survey of explosion models.

3.4 The Wind-Driven Shell

As the wind moves outward, it sweeps up the accreting gas, forming a high density peak significantly downstream of the forward shock, as seen in Figure 10. This peak steepens with time and eventually forms a secondary, reverse shock. We refer to the region in between the two shocks as the wind-driven shell.

Figure 9 shows the radius of the forward and reverse shocks as a function of time. We see that the shocks quickly approach a constant velocity, and that the reverse shock moves more slowly than the forward shock – the wind-driven shell grows larger over time. This behavior is qualitatively similar to wind emergence seen in supernova models such as Burrows et al. (1995); Janka & Müller (1996).

3.5 Time-Dependent Perturbations

Here we investigate the stability of various configurations to time-dependent perturbations of $\dot{M}_{acc}$. We take initially stable configurations near, but below the critical curve, and reduce the mass accretion rate by a factor $f_{\dot{M}}$ for a short time $\Delta t_{\dot{M}}$. We find that there is a threshold for the duration of this perturbation, below which, no explosion is produced despite the fact that the configuration is unstable for finite time. Our results are summarized in Figure 11. We see that the critical $\Delta t_{\dot{M}}$ changes quickly towards larger $f_{\dot{M}}$ (smaller perturbations), and changes more slowly towards smaller $f_{\dot{M}}$ (larger perturbations).

These perturbations can be viewed as analogous to perturbations caused by asphericities in the Si/O burning layers found in 2D and 3D progenitor models (Arnett & Meakin 2011; Couch & Ott 2013; Couch et al. 2015). These papers suggest characteristic perturbation magnitudes of 20 per cent in velocity, corresponding to an equal size perturbation in $\dot{M}$ in our model ($f_{\dot{M}} = 0.8$).

We find no evidence for oscillatory solutions, whether stable (i.e., remaining constant in amplitude) or unstable (i.e., increasing in amplitude until the critical curve is crossed), such as those found in Gabay et al. (2015) and Fernández (2012). However, as our polytropic EOS does not have any radially dependent heating or cooling terms, our lack of evidence is not in conflict with the Gabay et al. (2015) or Fernández (2012) results.

4 CONCLUSION

We perform simulations of simple supernova models with a polytropic equation of state in an effort to extend the
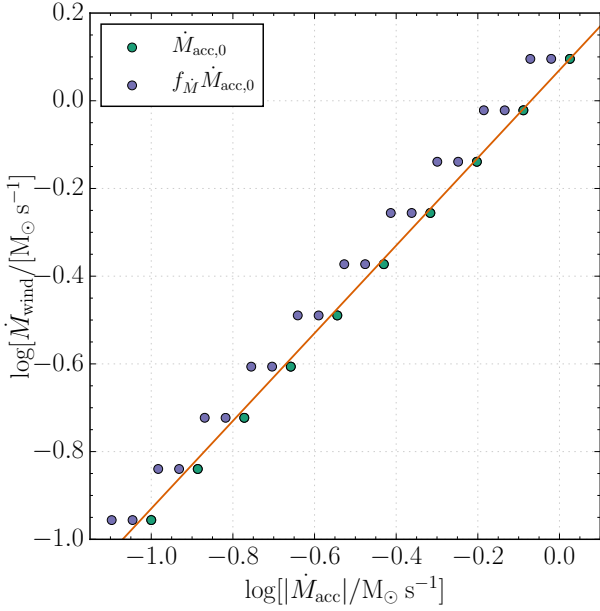
Figure 7. The wind mass loss rate $\dot{M}_{\rm wind}$ of the wind as a function of the accretion rate $\dot{M}_{\rm acc}$, for $\Gamma = 1.1$. The simulations here all have initial conditions on the critical curve. The green points show the initial mass accretion rate $\dot{M}_{\rm acc,0}$, while the blue points show the modified accretion rate, after being changed by the factor $f_{\dot{M}}$. The orange line shows the $\dot{M}_{\rm wind} \propto \dot{M}_{\rm acc}$ curve normalized to the highest $\dot{M}_{\rm acc}$ simulation. We see that the wind mass loss rate does not depend on $f_{\dot{M}}$ – each pair of simulations with the same $\dot{M}_{\rm acc,0}$ but differing $f_{\dot{M}}$ have the same $\dot{M}_{\rm wind}$. We further find that the analytical model (Equation 24) is a close but imperfect estimate of the numerical result – the relationship between $\dot{M}_{\rm wind}$ and $\dot{M}_{\rm acc}$ is very slightly superlinear, an effect we attribute to resolution.

Figure 8. The kinetic power $\dot{E} = \frac{1}{2}\dot{M}v^2$ of the transonic wind, measured at the sonic point, versus that of the accretion flow, measured at the shock immediately before explosion (i.e., at $t = t_{\rm wind}$). The orange line shows the $\dot{E}_{\rm wind} \propto \dot{E}_{\rm acc}$ curve normalized to the highest $\dot{E}_{\rm acc}$ simulation. The simulations support a linear relationship between $\dot{E}_{\rm wind}$ and $\dot{E}_{\rm acc}$.

findings of Pejcha & Thompson (2012) to time-dependent models. Our findings are as follows:

(i) We extend the analytic results of PT12 to derive a critical condition for a polytropic EOS (Equation 2, Figure 1, and Appendix A).

(ii) We verify the existence of the antesonic condition in time-dependent simulations, and that it is the same as the time-steady antesonic condition (§3.1; Figure 2 and Figure 6). In particular, when the antesonic condition is exceeded, we observe a time-dependent evolution from accretion to a thermally driven wind (§3.3; §3.4; Figure 3; Figure 10).

(iii) The value of the adiabatic index Γ has a strong effect on the length and time scales of the evolution of the explosion. Simulations using $\Gamma = 1.4$ have significantly larger critical shock radii than simulations with $\Gamma = 1.1$ do, and evolve more slowly (§3.1; Figure 4).

(iv) High resolution is required to fully capture the nature of the critical condition for explosion. At low resolutions, the critical curve is shifted to higher K. Configurations that explode at high resolution fail to do so at lower resolution. Only the highest resolutions found in the literature would yield accuracy $\lesssim 10$ per cent in the antesonic ratio or shock
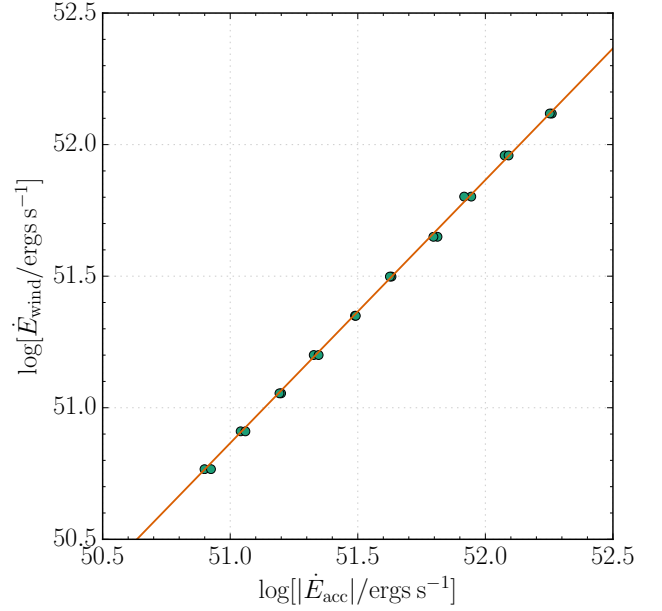
radius at the critical curve, under our model (§3.2; Figure 5 and Figure 6).

(v) There is an important physical connection between the mass loss rate of the post-explosion wind and the pre-explosion mass accretion rate of the PNS, for configurations that cross the critical curve (Figure 7). In particular, the mass loss rate of the transonic wind is proportional to the initial accretion rate. Furthermore, the kinetic power output of the wind is proportional to the kinetic power of accretion immediately before explosion (Figure 8). This result implies that higher accretion rate leads to an explosion with a larger wind mass loss rate and thus more kinetic power in the wind. All else being equal, these imply a larger total explosion energy, a larger nickel mass yield, and a *smaller* neutron star remnant (§3.3).

(vi) Our model supernovae are sensitive to time-dependent perturbations. We find that temporary decreases in the mass accretion rate can lead to explosion, even when the length of the perturbation is much smaller than the time required for the supernova to transition to the wind phase (§3.5; Figure 11).

Future work in this area will study the time-dependent antesonic condition in the presence of additional physics (e.g., rotation and magnetic fields), in multiple dimensions, and with a physical equation of state (explicitly including neutrino heating and cooling).
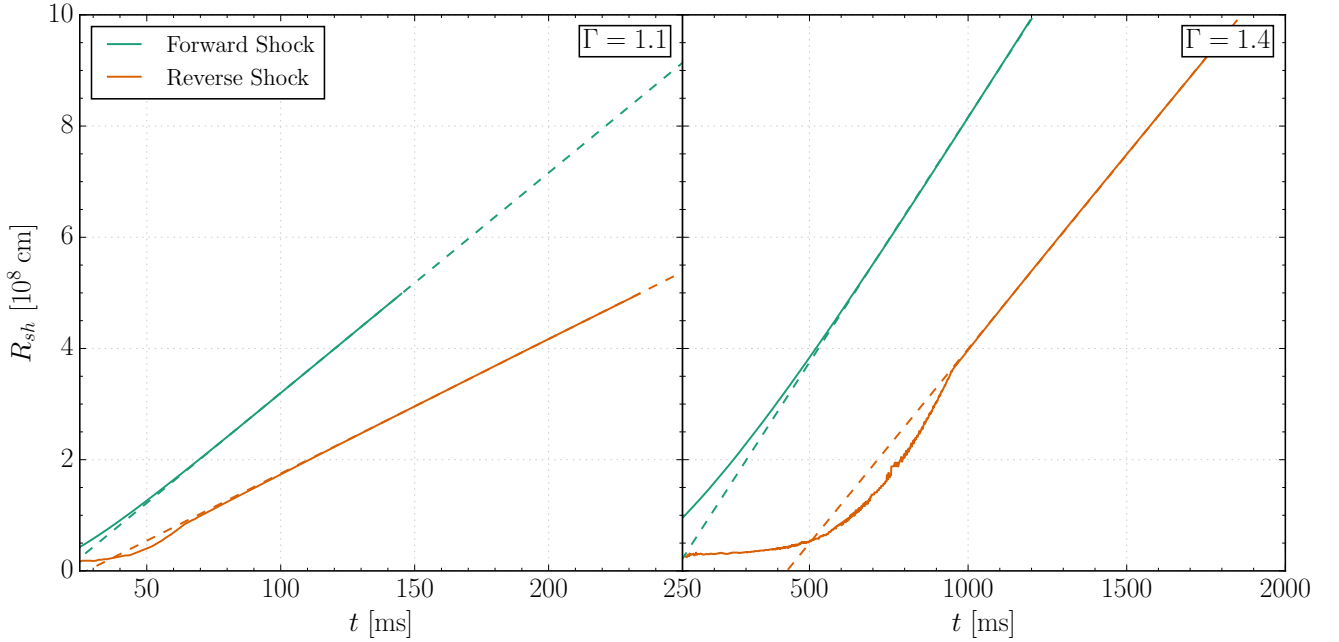
Figure 9. The radii of the forward and reverse shocks as a function of time, for $\Gamma = 1.1$ (left) and $\Gamma = 1.4$ (right), for $\dot{M}_{\rm acc,0} = 1.06 M_\odot \rm s^{-1}$. Dashed lines show linear fits to the later t points; we see that the shock expansion is linear at these times – i.e., that the shock velocity is constant.
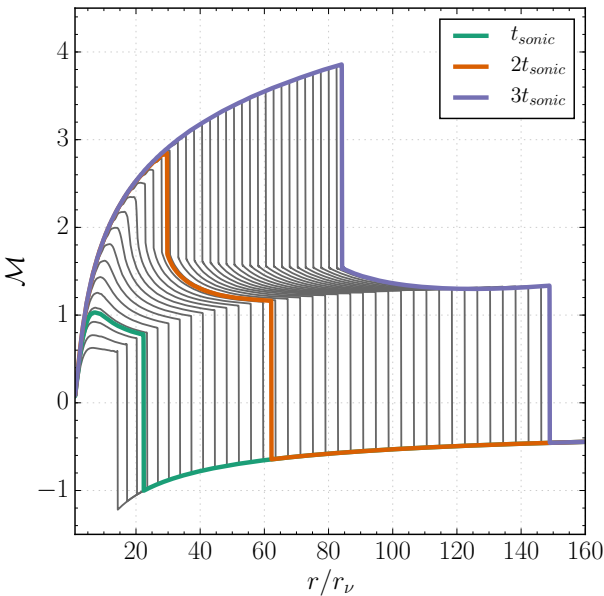

Figure 10. Velocity profiles for the $\dot{M}_{\rm acc,0} = 1.06\,M_\odot\,\rm s^{-1}$ and $\Gamma = 1.1$ model, as per Figure 3, but showing $t \gtrsim t_{\rm sonic}$ instead. As before, the profile highlighted in blue corresponds to $t = t_{\rm sonic}$.

5   ACKNOWLEDGEMENTS

REFERENCES

Arnett W. D., Meakin C., 2011, ApJ, 733, 78
Bethe H. A., Wilson J. R., 1985, ApJ, 295, 14
Blondin J. M., Mezzacappa A., DeMarino C., 2003, ApJ, 584, 971
Burrows A., Goshy J., 1993, ApJ, 416, L75
Burrows A., Hayes J., Fryxell B. A., 1995, ApJ, 450, 830
Couch S. M., 2013, ApJ, 775, 35
Couch S. M., Ott C. D., 2013, ApJ, 778, L7
Couch S. M., Chatzopoulos E., Arnett W. D., Timmes F. X., 2015, ApJ, 808, L21
Dolence J. C., Burrows A., Zhang W., 2015, ApJ, 800, 10
Ertl T., Janka H.-T., Woosley S. E., Sukhbold T., Ugliano M., 2016, ApJ, 818, 124
Fernández R., 2012, ApJ, 749, 142
Fernández R., 2015, MNRAS, 452, 2071
Fernández R., Thompson C., 2009, ApJ, 697, 1827
Foglizzo T., Scheck L., Janka H.-T., 2006, ApJ, 652, 1436
Fryxell B., et al., 2000, ApJS, 131, 273
Gabay D., Balberg S., Keshet U., 2015, ApJ, 815, 37
Herant M., Benz W., Hix W. R., Fryer C. L., Colgate S. A., 1994, ApJ, 435, 339
Hunter J. D., 2007, Computing In Science & Engineering, 9, 90
Janka H.-T., Müller E., 1995, ApJ, 448, L109
Janka H.-T., Müller E., 1996, Astronomy and Astrophysics
Lentz E. J., et al., 2015, ApJ, 807, L31
Murphy J. W., Burrows A., 2008, ApJ, 688, 1159
Murphy J. W., Dolence J. C., 2017, ApJ, 834, 183

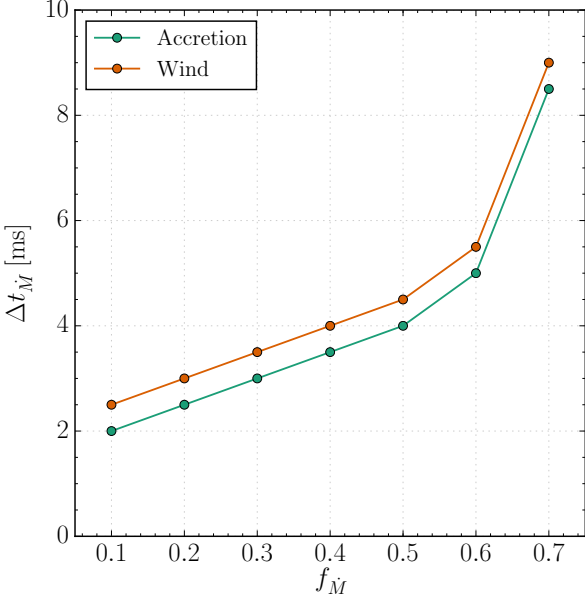a supernova explosion). By definition, the $\mathcal{M}$ profile of this solution must be tangent to $\mathcal{M}^-$ at the point of intersection. Thus, we can find the critical antesonic ratio by determining the antesonic ratio for which $\frac{\partial \mathcal{M}}{\partial \xi} = \frac{\partial \mathcal{M}^-}{\partial \xi}$.

We can write $\frac{\partial \mathcal{M}}{\partial \xi}$ as:

$$\frac{\partial \mathcal{M}}{\partial \xi} = \frac{\partial \mathcal{M}}{\partial r}\frac{\partial r}{\partial \xi} = \frac{1}{c_s}\left(\frac{\partial v}{\partial r} - \mathcal{M}\frac{\partial c_s}{\partial r}\right)\frac{\partial r}{\partial \xi}, \qquad \text{(A1)}$$

where ξ is the antesonic ratio:

$$\xi = \frac{c_s^2 r}{2GM}. \qquad \text{(A2)}$$

Thus we can write:

$$\frac{\partial \xi}{\partial r} = \frac{c_s^2 r}{2GM}\left(\frac{1}{r} + \frac{2}{c_s}\frac{\partial c_s}{\partial r}\right) \qquad \text{(A3)}$$

$$\frac{\partial r}{\partial \xi} = \left(\frac{\partial \xi}{\partial r}\right)^{-1} = \frac{1}{\xi}\left(\frac{1}{r} + \frac{2}{c_s}\frac{\partial c_s}{\partial r}\right)^{-1} \qquad \text{(A4)}$$

$$\frac{\partial r}{\partial \xi} = \frac{c_s r}{\xi}\left(c_s + 2r\frac{\partial c_s}{\partial r}\right)^{-1}, \qquad \text{(A5)}$$

and thus:

$$\frac{\partial \mathcal{M}}{\partial \xi} = \frac{r}{\xi}\frac{\frac{\partial v}{\partial r} - \mathcal{M}\frac{\partial c_s}{\partial r}}{c_s + 2r\frac{\partial c_s}{\partial r}}. \qquad \text{(A6)}$$

From Equation 11, we can determine:

$$\frac{\partial \mathcal{M}_-}{\partial \xi} = \frac{1 - \sqrt{\frac{\Gamma}{\Gamma - 4\xi}}}{4\xi^{3/2}}. \qquad \text{(A7)}$$

Thus, the critical condition can be written as:

$$\frac{\partial \mathcal{M}}{\partial \xi} - \frac{\partial \mathcal{M}_-}{\partial \xi} = 0, \qquad \text{(A8)}$$

$$\frac{r}{\xi}\frac{\frac{\partial v}{\partial r} - \mathcal{M}\frac{\partial c_s}{\partial r}}{c_s + 2r\frac{\partial c_s}{\partial r}} - \frac{1 - \sqrt{\frac{\Gamma}{\Gamma - 4\xi}}}{4\xi^{3/2}} = 0. \qquad \text{(A9)}$$

For convenience, we rewrite the Euler equations (Equation 4 and Equation 5) in the form:

$$\frac{\partial \rho}{\partial r} = -\frac{\rho}{2r}\frac{\xi^{-1} - 4\mathcal{M}^2}{1 - \mathcal{M}^2}, \qquad \text{(A10)}$$

$$\frac{\partial v_r}{\partial r} = \frac{v_r}{2r}\frac{\xi^{-1} - 4}{1 - \mathcal{M}^2}. \qquad \text{(A11)}$$

Assuming a polytropic equation of state, the sound speed is

$$c_s^2 = \frac{\partial P}{\partial \rho} = \frac{\partial}{\partial \rho}(K\rho^\Gamma) = K\Gamma\rho^{\Gamma - 1}, \qquad \text{(A12)}$$

and thus we have:

$$\frac{\partial c_s}{\partial r} = \frac{\partial}{\partial r}\left(\sqrt{K\Gamma\rho^{\Gamma - 1}}\right) \qquad \text{(A13)}$$

$$\frac{\partial c_s}{\partial r} = \frac{\Gamma - 1}{2}\frac{c_s}{\rho}\frac{\partial \rho}{\partial r} \qquad \text{(A14)}$$

$$\frac{\partial c_s}{\partial r} = \frac{\Gamma - 1}{4}\frac{c_s}{r}\frac{\xi^{-1} - 4\mathcal{M}^2}{1 - \mathcal{M}^2}. \qquad \text{(A15)}$$

The critical condition (Equation A9) is thus exactly given by

$$\frac{\mathcal{M}_-}{\xi}\frac{\frac{\Gamma + 1}{4\xi} - 2 - \mathcal{M}_-^2(\Gamma - 1)}{\mathcal{M}_-^2(2\Gamma - 3) + 1 - \frac{\Gamma - 1}{2\xi}} - \frac{1 - \sqrt{\frac{\Gamma}{\Gamma - 4\xi}}}{4\xi^{3/2}} = 0. \quad \text{(A16)}$$

Figure 11. Stability of the simulation against transient perturbations, for an initial accretion rate $\dot{M}_{\mathrm{acc},0} = 1.06\,\mathrm{M_\odot\,s^{-1}}$. The initial conditions correspond to a configuration on the critical curve. We see that for larger decreases in accretion rate (i.e., for smaller $f_{\dot{M}}$), the maximum stable perturbation time is smaller.

O'Connor E., Couch S., 2015, preprint (arXiv:1511.07443)
Pejcha O., Thompson T. A., 2012, ApJ, 746, 106
Pejcha O., Thompson T. A., 2015, ApJ, 801, 90
Radice D., Ott C. D., Abdikamalov E., Couch S. M., Haas R., Schnetter E., 2016, ApJ, 820, 76
Sukhbold T., Ertl T., Woosley S. E., Brown J. M., Janka H.-T., 2016, ApJ, 821, 38
Takiwaki T., Kotake K., Suwa Y., 2012, ApJ, 749, 98
Takiwaki T., Kotake K., Suwa Y., 2014, ApJ, 786, 83
Turk M. J., Smith B. D., Oishi J. S., Skory S., Skillman S. W., Abel T., Norman M. L., 2011, ApJS, 192, 9
Ugliano M., Janka H.-T., Marek A., Arcones A., 2012, ApJ, 757, 69
Yamasaki T., Yamada S., 2005, ApJ, 623, 1000
Yamasaki T., Yamada S., 2007, ApJ, 656, 1019

APPENDIX A: THE POLYTROPIC ANTESONIC CONDITION

An analytic expression for the antesonic condition can only be found for an isothermal equation of state. Even with a simple, polytropic equation of state, the equations become intractable.

However, consider a 'graphical' solution to the problem. When the velocity accretion profiles are plotted in the ξ-$\mathcal{M}$ space (such as in Figure 1), they must intersect the curve $\mathcal{M}^-$ (defined in Equation 11) if they have a shock. It stands to reason then that there must be a 'last' solution – a solution where any increase in K yields a solution that does not intersect $\mathcal{M}^-$ – i.e., a solution that doesn't have a shock, and, according to PT12, represents a configuration that *must* undergo a dynamical transition to a wind (i.e.,

We find the solution to the equation to be exactly

$$\xi_{\mathrm{crit}}^{\mathrm{poly}} = \frac{3}{16}\Gamma. \qquad (A17)$$